RIS-Assisted Full-Duplex Relay Systems

Sultangali Arzykulov, *Member, IEEE*, Galymzhan Nauryzbayev, *Senior Member, IEEE*, Abdulkadir Celik, *Senior Member, IEEE*, and Ahmed M. Eltawil, *Senior Member, IEEE*

***Abstract*—Reconfigurable intelligent surfaces (RISs) have recently been presented as a revolutionary technique and recognized as one of the candidates for beyond fifth-generation wireless networks. The RIS technology becomes especially attractive due to its capability to operate in a full-duplex (FD) mode, which is able to ideally double the half-duplex radio spectrum efficiency. This article analyzes the performance of an RIS-aided multihop FD relaying system, where an intermediate FD relay is employed to defeat the far-field path-loss effect inherent to RIS communication links. To this end, we analytically derive exact and asymptotic closed-form expressions for the outage probability, average spectral efficiency, and average bit error rate. The RIS-aided system demonstrates effective performance improvement for the proposed network. However, from the results, it is noticed that the increase in the number of RIS units within a certain communication link does not provide linear performance improvement due to the RIS channel's far-field path-loss model. Thus, mixing active FD relaying techniques with passive RIS platforms can be an ideal solution to improve further system performance, such as outage probability, average spectral efficiency, and average bit error rate in RIS-enabled networks.**

***Index Terms*—Bit error rate (BER), full-duplex (FD), outage probability (OP), reconfigurable intelligent surface (RIS), spectral efficiency.**

I. Introduction

FUTURE wireless networks will be required to provide a thousand times as much capacity increase compared to the current networks to support the quality of service (QoS) needed by high-data-rate applications, such as virtual reality and three-dimensional (3-D) video [1]. This enormous increase in data traffic cannot be obtained with the existing wireless communication systems. Hence, intensive research is being carried out by academia and industry to overcome the deficiencies of traditional transmission concepts. One of the promising technologies for future wireless networks is millimeter-wave (mmWave) communication that can provide gigabits-per-second communication rates by offering wider bandwidth [2]. The primary distinctive technical feature of the mmWave communication is that signals suffer from a significant path loss compared to conventional lower frequency bands. This severe path-loss effect in mmWave bands can be overcome using large antenna arrays [3], [4]. For this purpose, multiple-input multiple-output (MIMO) technology is employed to perform beamforming in order to obtain an array gain that overcomes the path-loss impact in an mmWave frequency range [5]. However, in dense urban and indoor areas, the mmWave communications' high directivity antennas become oversensitive to blockages [6]. In addition to this, mmWave frequency range still has restrictions in terms of propagation characteristics, such as diffraction, penetration loss, and scattering [6]. In recent years, reconfigurable intelligent surfaces (RISs) have been proposed to address the blockage issue and improve the coverage in mmWave communications [7]. The RIS is considered to be a key technique in the future beyond fifth-generation(5G) systems, which can be considered as a physical evolution of massive MIMO [8], where multiple reflecting antenna modules can be programmed to control the propagation environment in a constructive manner. Hence, the RIS provides the programmable control of the wireless medium [9]. The RIS can be easily integrated into the interior of buildings and on the surface of large vehicles with minor or no change of equipment and device software, which will significantly reduce the cost of performance improvement, e.g., power efficiency, connectivity, coverage extension, etc., for future wireless networks. Moreover, the RIS can be designed in a lightweight fashion due to its miniature circuitry, which makes it suitable for indoor propagation improvement [10]. The RIS has been studied for different wireless applications, namely, cognitive radio [11], wireless power transfer [12], nonorthogonal multiple access [13], wireless security [14], etc.

The operation principle of the RIS is similar to the full-duplex (FD) MIMO relay from the reflecting characteristic perspective. However, the RIS also refracts the incident signals by passing through its surface, which can effectively reconstruct the channels to blocked users and significantly improve transmission performance. Owing to these RIS characteristics, the RIS is believed to provide better system performance than that of half-duplex (HD)/FD relaying techniques. However, as numerically illustrated in [15], the RIS needs hundreds of reflecting elements and perfect phase-shifting ability to outperform a single-antenna HD decode-and-forward (DF) relay. Furthermore, it has been shown that a sufficiently large number of RIS elements are needed to outperform the FD-DF relay [16]. In addition, the RIS should be located at a short distance between the two nodes to provide maximum performance. The reason is that the source's signal passes through two hops before reaching the destination, which leads to a poor achieved channel gain due to the impact of a far-field path-loss effect [17]. One option to overcome the

Manuscript received 23 May 2021; revised 8 October 2021, 27 February 2022, and 30 April 2022; accepted 27 June 2022. Date of publication 26 July 2022; date of current version 9 December 2022. This work was supported by the Nazarbayev University under Collaborative Research Program Grant 11022021CRP1513 (PI: Galymzhan Nauryzbayev) and Social Policy Grant. *(Corresponding author: Sultangali Arzykulov.)*

Sultangali Arzykulov, Abdulkadir Celik, and Ahmed M. Eltawil are with the Computer, Electrical, and Mathematical Sciences and Engineering Division, King Abdullah University of Science and Technology, Thuwal 23955-6900, Saudi Arabia (e-mail: sultangali.arzykulov@gmail.com; abdulkadir.celik@kaust.edu.sa; ahmed.eltawil@kaust.edu.sa).

Galymzhan Nauryzbayev is with the Department of Electrical and Computer Engineering, School of Engineering and Digital Sciences, Nazarbayev University, Kabanbay Batyr 53 Nur-Sultan 010000, Kazakhstan (e-mail: galymzhan.nauryzbayev@nu.edu.kz).

Digital Object Identifier 10.1109/JSYST.2022.3189850

impact of far-field path loss in RIS communications is to adopt intermediate FD relays that can work as repeaters/boosters of the RIS-assisted signals and enhance spectral efficiency.

The FD transceiver simultaneously transmits and receives in the same frequency band; thus, it has the potential to double the spectrum utilization compared to the traditional HD systems [18]–[20]. The promising spectral efficiency gain in the FD networks also brings challenges in practice as strong self-interference (SI) exists at the transceiver caused by the simultaneous transmission mode [21]. If these interference terms are left without being canceled/removed, it can significantly degrade the FD networks' performance by making FD perform worse than the HD one. Various SI suppression methods have been proposed in the literature, such as passive cancellation [21], analog and digital cancellations [22], etc. The combination of these interference suppression techniques allows suppressing the SI at the FD node down to the background noise floor by making it possible to use FD systems in practice [23]. An appealing advantage of a dual-hop FD relaying has been extensively investigated in different wireless applications, e.g., cognitive radio [24], device-to-device communications [25], massive MIMO [26], and mmWave networks [27]. Hence, a combination of RIS and FD techniques in a future wireless network infrastructure could help achieve a high data rate. In that network, the RIS can be reconfigured to constructively combine the reflected signals at the receiver and reduce the effect of SI at the FD receivers by boosting the desired signal [28].

A. Related Works

RIS-assisted FD systems have been studied in a few works [29]–[32], where all of them considered the FD ability at the terrestrial transmitter/receiver node or both the nodes. These works concluded that the RIS improves the coverage and boosts the signal-to-noise ratio (SNR) level in FD communication systems. Tian *et al.* [33] proposed an unmanned aerial vehicle as an FD transmitter to deliver signals to uplink and downlink users through the RIS. The results showed that the proposed scheme outperforms the HD-RIS mode. Moreover, the study of RIS with other technologies, such as a device-to-device network [34], physical layer security [35], and nonorthogonal multiple access [36], showed the usefulness of the FD mode to improve the system performance. Despite the considerable FD-RIS literature, only a small number of works concentrated on the RIS-assisted two-hop FD communication systems. For example, Abdullah *et al.* [37] proposed a hybrid FD-RIS communication network, where the FD relay and the RIS forwarded data to the end user. The results illustrated that the proposed system outperformed the RIS only and RIS-assisted HD relay networks. Ying *et al.* [38] proposed an architecture consisting of double side-by-side RISs connected through a relay working in an FD mode. The numerical results showed that the proposed model achieved a higher rate than that of the simple RIS and conventional relay techniques, especially at high frequencies. Another conclusion of the work is that the FD relay-assisted RIS system can provide a certain transmission rate with much fewer elements than a traditional RIS architecture.

The RIS may play a vital role in future wireless networks by providing benefits in terms of reliability and QoS. Specifically, the multihop RIS technique is a good candidate for coverage extension solutions in short-ranged mmWave communication networks. Even though various RIS-aided networks have been studied in recent years, there is a lack of research investigating multihop or cascaded RISs comprehensively. Initial work on the topic of cascaded RIS systems with two relaying RISs has been studied in [39]–[41] to show that the two-hop RIS architecture obtains multiplied beamforming gain compared to the conventional single-hop RIS benchmark. However, these studies do not consider multiple RISs (higher than two) to illustrate the performance limits using multiple RISs within a fixed communication link, e.g., outage probability (OP), bit error rate (BER), spectral efficiency, etc. Hence, whether the increase in the number of RISs within a certain communication link leads to further improve system performance remains unknown. A second question is an interaction between passive RIS and active FD systems to satisfy target system performance metrics, such as the BER or the receiver SNR.

B. Contributions

To address the challenges mentioned above, this article first considers a single RIS-assisted FD relaying network, where the communication is performed through the assistance of both RIS and FD relay. We provide an analytical derivation in terms of the OP, average spectral efficiency, and average BER for the considered system model. Furthermore, we consider two system model cases: 1) communication in a two-hop RIS system and one FD relay and 2) communication in a three-hop RIS network. Here, we numerically show the benefit of the former system model. The main contributions of this article can be summarized as follows.

1) We compare a cascaded multihop RIS system with a multihop RIS-assisted FD relaying. Here, we show that the increase in the number of RIS elements within a communication link does not provide considerable spectral efficiency improvement due to the RIS channel's far-field path-loss model. However, the RIS network can achieve better system performance in terms of spectral efficiency, OP, and BER if it uses an intermediate DF-FD relaying node to combat the path-loss effect. We also show that the network with the FD relay obtains the spectral efficiency of an ideal phase-shift mode at a smaller phase-shift resolution than the cascaded RIS system.
2) The works [28], [32], and [39] offered noncentral chi-square (NCCS) distribution based on a central limit theorem (CLT) to describe the statistical model of RIS-aided communication links. However, as it was demonstrated in [42], the NCCS distribution has limitations such as the significant divergence between theoretical and simulation results and the applicability of this distribution only when the RIS has a large number of reflecting elements. Hence, this study analytically investigates the RIS-assisted FD relaying network, where a channel to/from the RIS is modeled by the Nakagami-m random variable (RV) and the distribution of the cascaded Nakagami-m channels is approximated by the squared generalized-K (K_G) distribution [43], which is a more accurate approximation than the NCCS. The tightness of the K_G model is validated over Monte Carlo simulations.
3) We provide exact OP, average spectral efficiency, and average BER performance by deriving the cumulative distribution functions (CDFs) and probability density functions (PDFs) of the proposed two-hop network. Moreover, asymptotic expressions for the analytical performance

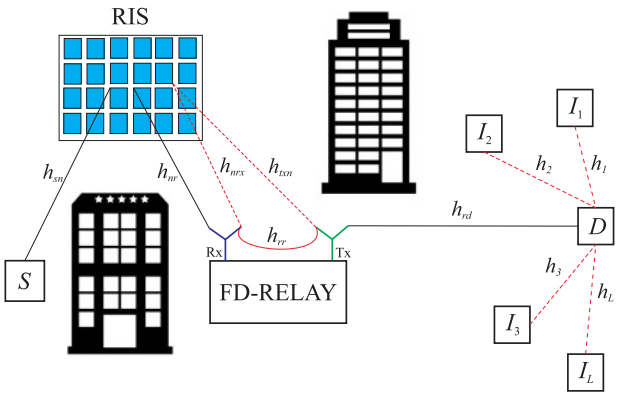

Fig. 1. Proposed RIS-assisted FD relay systems.

are provided in simple elementary function forms, which allow us to define the system's diversity order and attain further insights from the analytical studies. It is illustrated that the diversity order depends on the number of RIS elements and the wireless channel parameters.

The rest of this article is organized as follows. Section II introduces the system model and transmission protocol of an RIS-assisted FD relaying network. Section IV provides and discusses new closed form and approximated analytical expressions for the OP, average spectral efficiency, and average BER. Section V shows numerical findings to validate the correctness of theoretical analysis. Finally, Section VI concludes this article.

II. System Model

We consider an FD downlink transmission in an RIS-assisted network, which consists of a source node (S), an FD relay node (R), a destination node (D), and an RIS equipped with N reflecting elements (see Fig. 1). It is assumed that R operates under the DF relaying protocol,[1] and S and D are equipped with a single antenna, while R has one receive and one transmit antennas. Moreover, no direct link exists between S and R due to the presence of environmental obstacles. Thus, S sends a signal to D with the aid of RIS and R.

A. Channel Model

The channel coefficients[2] between the RIS's nth element and S/R are denoted by h_{sn}/h_{nr}, where $n \in \{1, 2, \ldots, N\}$. The RIS's each shifting element reflects the incoming signal with a reflection amplitude of $\eta \in [0, 1]$ and a phase-shift of $\theta \in [0, 2\pi)$. Furthermore, h_{rr} denotes the SI channel received directly at the receive antenna of R, while h_{txn}/h_{nrx} denotes the channel between the relay's transmit/receive antennas and the nth element of the RIS. Furthermore, h_{rd} denotes the channel between R and D, while h_l $\forall l \in \{1, 2, \ldots, L\}$ indicates an ambient interference channel to D. Measurement results in [44] showed that small-scale fading at mmWave is less severe than that in traditional bands, when narrow beam antennas are used. Therefore, similar to [45], we assume that the channel coefficient $h_j, j \in \{sn, nr, rr, rd, l\}$ is modeled by the Nakagami-m distribution with a following PDF:

$$f_Y(y) = \frac{2y^{2m_y-1}e^{-\frac{y^2}{\beta_y}}}{\Gamma(m_y)\beta_y^{m_y}}, \quad y \geq 0 \tag{1}$$

where $\Gamma(\cdot)$ is the Gamma function [46, eq. (8.310)] and m and β are the shape and the degree of fading severity parameters of the Nakagami-m fading distribution, respectively. For example, $m = 1$ represents Rayleigh fading, while $m \to \infty$ indicates a lack of fading. In the mmWave channel, the line-of-sight (LOS) component is less severe due to the less number of scatterers. Thus, the LOS component can be described by large m, while the non-LOS (NLOS) is characterized by smaller m.

B. Source-to-Relay Link

By expressing the channel coefficients as $h_{sn} = |h_{sn}|e^{-j\psi_n}$ and $h_{nr} = |h_{nr}|e^{-j\phi_n}$, where $|h_{sn}|$ and $|h_{nr}|$ denote the channel amplitudes, which follow the Nakagami-m distribution, while ψ_n and ϕ_n are the channel phases, we can write the signal received at R via the RIS as

$$y_R = \underbrace{\sum_{n=1}^{N} \sqrt{\frac{P_s}{d_{sn}^{\tau} d_{nr}^{\tau}}} \eta_n |h_{sn}| |h_{nr}| e^{j(\theta_n - \psi_n - \phi_n)} x_d}_{\text{SOI}} + n_r + \underbrace{\sqrt{P_{\text{SI}}} h_{rr} x_{\tilde{d}}}_{\text{SI}} + \underbrace{\sum_{n=1}^{N} \sqrt{\frac{P_r}{d_{txn}^{\tau} d_{nrx}^{\tau}}} \eta_n e^{j\theta_n} h_{txn} h_{nrx} x_{\tilde{d}}}_{\text{SI from RIS}} \tag{2}$$

where P_ι, with $\forall \iota \in \{S, R\}$, is the transmit power at node ι; P_{SI} is the SI power at R; d_{sn} indicates the distance of the S-RIS link, while d_{nr} is the distance from the RIS to R; d_{txn} and d_{nrx} denote the distances from the relay's transmit and receive antenna to the RIS, respectively; $\eta_n \in [0, 1]$ and $\theta_n \in [0, 2\pi)$ denote the amplitude reflection coefficient and the effective phase shift introduced by the RIS's nth element, respectively; and τ is the path-loss coefficient. Moreover, signal of interest (SOI) and SI messages are represented by x_d and $x_{\tilde{d}}$, with $\mathbb{E}(|x_d|^2) = \mathbb{E}(|x_{\tilde{d}}|^2) = 1$, respectively.

We consider an interference-limited network, where the effect of the additive white Gaussian noise (AWGN) is negligible [47]. Furthermore, considering the principle of the RIS to constructively beamform the signal in desired directions and suppress interference by spatial filtering [48], we assume that there is no interference from the RIS to R [49]. In addition, we also assume that interference at R from interference nodes is neglected compared to the strong SI loop[3] [28]. In light of the above discussions and for the sake of analytical tractability, we rewrite the signal-to-interference ratio (SIR) at R as

$$\gamma_R = \frac{\left|\sum_{n=1}^{N} \bar{P}_s \eta_n |h_{sn}| |h_{nr}| e^{j(\theta_n - \psi_n - \phi_n)}\right|^2}{P_{SI} |h_{rr}|^2} \tag{3}$$

[1]We consider the DF relaying mode as the amplify-and-forward scheme achieves lower performance due to its noise amplification feature [15].

[2]Similar to [12], [14], and [30], we also assume that channel state information is available to all the users, and the results derived can be considered as the performance upper bound.

[3]We justify our assumptions of ignoring the negligible effect of AWGN in the interference-limited network and interference in the FD relay in Section V.

where $\bar{P}_s = \sqrt{\frac{P_s}{d_{sn}^{\tau} d_{nr}^{\tau}}}$. The maximum SIR value can be obtained by setting $\eta_n = 1$ and the reflected signals need to be cophased[4] by $\theta_n = \psi_n + \phi_n$. Thus, the maximum SIR at R can be written as

$$\gamma_R = \frac{W}{Y} \tag{4}$$

where $W = \bar{P}_s Z^2$; $Z = \sum_{n=1}^{N} X$ and $X = |h_{sn}||h_{nr}|$ is double Nakagami-m RV. Moreover, $Y = P_{\text{SI}}|h_{rr}|^2$ is the gamma-distributed RV with shape and scale parameters of Gamma$(m_y, \bar{\beta}_y)$, where $\bar{\beta}_y = P_{\text{SI}}\beta_y$.

The double Nakagami-m RV X can be presented over the K_G distribution [43]. Moreover, as it is stated in [43, eq. (1)], the PDF of the sum of several K_G RVs is well approximated by $\sqrt{U}$, with $U = \sum_{n=1}^{N} X^2$. Hence, we express the PDF of the RV Z as follows:

$$f_Z(z) = \frac{4\Psi^{k_w+m_w}}{\Gamma(k_w)\Gamma(m_w)} z^{k_w+m_w-1} K_{k_w-m_w}(2\Psi z) \tag{5}$$

where $K_t(\cdot)$ is the modified t-order Bessel function of the second kind [46, eq. (8.432)], $\Psi = \sqrt{\frac{k_w m_w}{\Omega_w}}$, and $\Omega_w = \mathbb{E}[Z^2]$; $m_w = \frac{-b+\sqrt{b^2-4ac}}{2a}$ and $k_w = \frac{-b-\sqrt{b^2-4ac}}{2a}$ are the real-valued shaping parameters. However, if these parameters are complex conjugate numbers, they can be set to the magnitude of the estimated complex parameters. Furthermore, parameters a, b, and c are given in [43] and can be calculated using the kth moments of Z as

$$\mathbb{E}[Z^k] = \sum_{n_1=0}^{k} \sum_{k_2=0}^{k_1} \cdots \sum_{k_{N-1}=0}^{k_{N-2}} \binom{k}{k_1}\binom{k_1}{k_2}\binom{k_{N-2}}{k_{N-1}} \times \mathbb{E}[X_1^{k-k_1}]\mathbb{E}[X_2^{k_1-k_2}]\cdots\mathbb{E}[X_{N-1}^{k_{N-1}}] \tag{6}$$

where $\mathbb{E}[X_j^k]$ is the kth moment of X_i, which is derived as [50, eq. (9)]

$$E[X_j^k] = \prod_{p=1}^{2} \frac{\Gamma\left(m_p + \frac{k}{2}\right)}{\Gamma(m_p)} \left(\frac{\beta_p}{m_p}\right)^{k/2}. \tag{7}$$

From (4) and (5), the PDF of the RV W can be expressed as the squared K_G distribution[5] as follows:

$$f_W(w) = \frac{2\bar{\Psi}^{k_w+m_w} w^{\frac{k_w+m_w}{2}-1}}{\Gamma(m_w)\Gamma(k_w)} K_{k_w-m_w}\left(2\bar{\Psi}\sqrt{w}\right) \tag{8}$$

where $\bar{\Psi} = \sqrt{\Psi/\bar{P}_s}$. Then, the CDF of (8) is derived as [42]

$$F_W(w) = \frac{1}{\Gamma(m_w)\Gamma(k_w)} G_{1,3}^{2,1}\left[\bar{\Psi}^2 w \middle| \begin{matrix} 1 \\ k_w, m_w, 0 \end{matrix}\right] \tag{9}$$

where $G_{\cdot,\cdot}^{\cdot,\cdot}[\cdot]$ denotes the Meijer G-function [46, eq. (9.301)].

[4]We consider perfect signal cophasing to make the analytical derivations tractable. We also provide a system model with imperfect phase shifting due to the RIS phase shifter's quantization error in numerical results.

[5]It has been proven for the RIS channel models that the squared K_G distribution is more accurate than the CLT-based NCCS distribution [42].

C. Relay-to-Destination Link

The instantaneous SIR of the R–D link can be written as $\gamma_D = \frac{V}{U}$, where $V = \frac{P_r}{d_{rd}^{\tau}}|h_{rd}|^2$ is the Gamma-distributed RV, $U = \sum_{l=1}^{L} \frac{P_l}{d_l^{\tau}}|h_l|^2$ is the summation of L independent but not identically distributed Gamma RVs, P_l is the transmit power at interference node l, and d_l denotes the distance from interfering node l to D. The PDF of U can be closely approximated by [51]

$$f_U(u) = \frac{u^{\tilde{m}_u-1} e^{-\frac{u}{\tilde{\beta}_u}}}{\Gamma(\tilde{m}_u)\tilde{\beta}_u^{\tilde{m}_u}} \tag{10}$$

where the approximated scale parameter $\tilde{\beta}_u$ is evaluated by solving a set of equations, $\frac{\mu}{2} - 2\sum_{l}^{L} \frac{m_l \beta_t^3}{(\beta_l+\tilde{\beta}_u)^2} = 0$, $\mu = \sum_{l=1}^{L} m_l\beta_l$, and the shape parameter is given by $\tilde{m}_u = \frac{\mu}{\tilde{\beta}_u}$.

III. Cascaded Multihop RIS System

This section considers a multihop RIS-assisted cooperative communication system, as shown in Fig. 2, where we assume that, due to the severe blockage by obstacles, there is no direct link and interference leakage at each RIS from the rest RISs. We consider two system models, namely, Cases I and II.

Case I: The S-to-D communication happens through two RISs and one intermediate the FD relay node. In this case, the end-to-end spectral efficiency is a function of SINR received at FD relay and D. The received SINR at the FD relay is identical to (3), while the SINR at D, considering the cascaded RIS channel, can be written as

$$\gamma_D^I = \frac{P_r \left|\sum_{q=1}^{Q} \frac{\eta_q}{d_{rq}^{\tau} d_{qd}^{\tau}} |h_{rq}||h_{qd}| e^{j(\theta_q-\psi_q-\phi_q)}\right|^2}{U} \tag{11}$$

where the channel coefficients between the RIS B's qth element and R/D are denoted by h_{rq}/h_{qd}. Therefore, the spectral efficiency for Case I can be written as

$$C^I = \log_2\left(1 + \min\left(\gamma_R, \gamma_D^I\right)\right). \tag{12}$$

Case II: The communication in Case II occurs through a cascaded three RISs and the end-to-end spectral efficiency is a function of received SINR at D, which can be written as in (13), shown at the bottom of the next page.

Then, the spectral efficiency for Case II can be written as

$$C^{II} = \log_2\left(1 + \gamma_D^{II}\right). \tag{14}$$

To the best of the authors' knowledge, the channel distribution model of cascaded multihop RIS communication links has not been studied and is still a challenging research topic. Therefore, we consider the performance of the multihop RIS system numerically in Section V to show that the intermediate FD relay can improve the spectral efficiency of the cascaded RIS communication link.

IV. Performance Analysis

This section provides closed-form solutions for the OP, average spectral efficiency, and average BER for the proposed RIS-aided FD network in Fig. 1. Besides, asymptotic equations at high transmit power are calculated to gain more technical insights into the system performance.

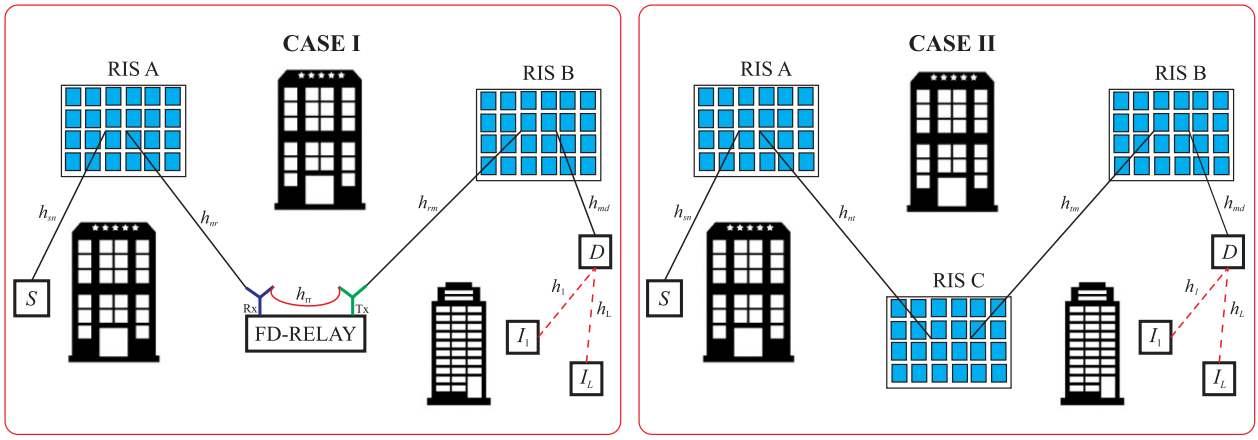

Fig. 2. Communication through the FD relay as intermediate node (Case I) and through cascaded three RISs (Case II).

A. Outage Probability

The OP performance can assess the reliability of the communication link. The OP happens when the instantaneous SIR is below a predefined threshold $\bar{\gamma}$. Hence, the end-to-end OP at D is written as [52]

$$P_{\text{out}}(\bar{\gamma}) \triangleq F_{\gamma}(\bar{\gamma}) = \Pr\left[\min\left(\gamma_R, \gamma_D\right) < \bar{\gamma}\right] = F_{\gamma_R}(\bar{\gamma}) + F_{\gamma_D}(\bar{\gamma}) - F_{\gamma_R}(\bar{\gamma}) F_{\gamma_D}(\bar{\gamma}). \quad (15)$$

Lemma 1: The end-to-end OP at the destination node can be written as in (16), shown at the bottom of this page.

Proof: We refer interested readers to Appendix A for the derivation steps. ■

Since (16) expresses the OP in the form of the Meijer G-function, it may be limited to provide a deep engineering insight into the outage behavior of an end-to-end system. Therefore, the asymptotic analysis is considered by setting $P_s = P_r \to \infty$ to indicate diversity gain and attain more useful information regarding the overall system performance. By using [53, eq. (07.34.06.0040.01)] for Meijer G-functions in (16), we can express the asymptotic OP as

$$P^{\infty}_{\text{out}}(\bar{\gamma}) \approx F^{\infty}_{\gamma_R}(\bar{\gamma}) + F^{\infty}_{\gamma_D}(\bar{\gamma}) \approx \frac{\Delta_r \Gamma(|m_w - k_w|)}{t\left(\bar{\gamma}\bar{\Psi}^2\bar{\beta}_y\right)^{-t}}\Gamma(m_y + t) + \frac{\Delta_d \Gamma(m_v)\Gamma(m_v + \tilde{m}_u)}{m_v}\left(\frac{\tilde{\beta}_u}{\bar{\beta}_v}\bar{\gamma}\right)^{m_v} \quad (17)$$

where $t = \min(m_w, k_w)$. In addition, (17) indicates that the achievable diversity order is $\min(m_w, k_w, m_v)$. Moreover, as m_w and k_w are defined from the number of RIS's shifting elements, the diversity order also depends on N.

B. Average Spectral Efficiency

The end-to-end average spectral efficiency of the considered system model can be expressed as [54, eq. (15)]

$$C = \frac{1}{\ln(2)}\int_0^{\infty} \ln\left(1 + \bar{\gamma}\right) f_{\gamma}(\bar{\gamma}) d\bar{\gamma}. \quad (18)$$

The end-to-end PDF $f_{\gamma}(\bar{\gamma})$ in (18) can be derived by

$$f_{\gamma}(\bar{\gamma}) = f_R(\bar{\gamma}) + f_D(\bar{\gamma}) - f_R(\bar{\gamma})F_D(\bar{\gamma}) - f_D(\bar{\gamma})F_R(\bar{\gamma}) \quad (19)$$

where $f_R(\bar{\gamma})$ and $f_D(\bar{\gamma})$ are the respective PDFs of γ_R and γ_D.

Lemma 2: The end-to-end average spectral efficiency for D is written in closed form as in (20), shown at the bottom of the next page.

Proof: The detailed derivation of the average spectral efficiency is given in Appendix B. ■

C. Average BER

The average BER for some modulation schemes can be calculated as [55, eq. (25)]

$$P_e = \frac{q^p}{2\Gamma(p)}\int_0^{\infty} \bar{\gamma}^{p-1} e^{-q\bar{\gamma}} F_{\gamma}(\bar{\gamma}) d\bar{\gamma} \quad (21)$$

$$\gamma_D^{II} = \frac{P_r \left|\sum_{q=1}^{Q} \frac{\eta_q}{d_{qd}^{\tau}} |h_{qd}| e^{j(\theta_q - \phi_q)} \sum_{t=1}^{T} \frac{\eta_{tq}}{d_{tq}^{\tau}} |h_{tq}| e^{j(\theta_{tq} - \phi_{tq})} \sum_{n=1}^{N} \frac{\eta_{nt}}{d_{sn}^{\tau} d_{nt}^{\tau}} |h_{sn}| |h_{nt}| e^{j(\theta_{nt} - \psi_{sn} - \phi_{nt})}\right|^2}{U} \quad (13)$$

$$P_{\text{out}}(\bar{\gamma}) = \Delta_r G_{2,3}^{2,2}\left[\frac{\bar{\gamma}\bar{\beta}_y}{\bar{\Psi}^{-2}}\middle| \begin{matrix} 1, 1 - m_y \\ k_w, m_w, 0 \end{matrix}\right] + \Delta_d G_{2,2}^{1,2}\left[\frac{\tilde{\beta}_u}{\bar{\beta}_v}\bar{\gamma}\middle| \begin{matrix} 1, 1 - \tilde{m}_u \\ m_v, 0 \end{matrix}\right] - \Delta_r\Delta_d G_{2,3}^{2,2}\left[\frac{\bar{\gamma}\bar{\beta}_y}{\bar{\Psi}^{-2}}\middle| \begin{matrix} 1, 1 - m_y \\ k_w, m_w, 0 \end{matrix}\right] G_{2,2}^{1,2}\left[\frac{\tilde{\beta}_u}{\bar{\beta}_v}\bar{\gamma}\middle| \begin{matrix} 1, 1 - \tilde{m}_u \\ m_v, 0 \end{matrix}\right] \quad (16)$$

where the values of p and q depend on a modulation scheme chosen. For instance, binary phase-shift keying and differential phase-shift keying (DPSK) are obtained by setting $p = 0.5/q = 1$ and $p = 1/q = 1$, respectively.

Lemma 3: The end-to-end average BER for D can be written in closed form as in (22), shown at the bottom of this page.

Proof: See Appendix C. ■

The asymptotic average BER can be found by inserting the CDFs in (17) into (21) and, after some mathematical manipulations, can be derived as

$$\begin{aligned} P_e^{\infty} &\approx \frac{q^p}{2\Gamma(p)} \int_0^{\infty} \bar{\gamma}^{p-1} e^{-q\bar{\gamma}} \left(F_{\gamma_R}^{\infty}(\bar{\gamma}) + F_{\gamma_D}^{\infty}(\bar{\gamma}) \right) \mathrm{d}\bar{\gamma} \\ &\approx \frac{q^p \Delta_r}{2\Gamma(p)} \frac{\Gamma(|m_w - k_w|)\Gamma(m_y + t)\Gamma(p+t)}{t \left(\bar{\Psi}^2 \bar{\beta}_y\right)^{-t} q^{p+t}} \\ &\quad + \frac{q^p \Delta_d}{2\Gamma(p)} \frac{\Gamma(m_v)\Gamma(m_v + \tilde{m}_u)\Gamma(p+m_v)}{m_v q^{p+m_v}} \left(\frac{\tilde{\beta}_u}{\bar{\beta}_v} \right)^{m_v}. \end{aligned} \tag{23}$$

It is worth noting that the asymptotic outage (17) and BER (23) are expressed in terms of elementary functions, which do not require advanced software to compute.

V. Numerical Results

This section presents numerical results to investigate the impact of key system parameters on the end-to-end system performance. Monte Carlo simulations based on the interference-limited system model discussed in Section II are used to verify the correctness of the analytical derivations. We consider the system parameters shown in Table I, unless stated otherwise. Moreover, the following 2-D plane locations are considered: S is located at the origin $\{x_s; y_s\} = \{0; 0\}$, while the RIS and R are located at $\{x_{ris}; y_{ris}\} = \{50; 10\}$ and $\{x_r; y_r\} = \{100; 0\}$ m, respectively. Finally, D resides at $\{x_d; y_d\} = \{150; 0\}$ m[6].

TABLE I
Default System Parameters

Parameter	Value
Predefined threshold, $\bar{\gamma}$	3 dB
Residual SI power at R[6]	-60 dB
Path-loss coefficient for links to/from RIS	2.2
Path-loss coefficient for $R-D$ link	2.7
Number of randomly located interference nodes, L	5

In Fig. 3, we demonstrate some results of the OP, average spectral efficiency, and average BER[7] for the proposed FD-RIS system with a different number of RIS elements, N. It is clearly observed that the analytical results obtained using the K_G approximation provide highly tight consistency with the simulation results. In Fig. 3(a), we can observe that the outage performance improves by N. Moreover, it is worth noting that the analytical results are tighter with the simulation ones when the RIS has a higher number of reflecting elements.

Similarly, Fig. 3(b) shows that an increase of N helps obtain better average spectral efficiency, which justifies using RIS in the FD-based networks. However, for the considered FD-RIS model setup, the outage and spectral efficiency results show the advantage of using the RIS only when $N \geq 16$. This is due to the far-field channel modeling of RIS communication link, where the RIS with a lower number of reflecting elements is vulnerable to the path-loss impact. However, this impact can be diminished by using the RIS with a larger N, which improves the SNR at the receiving node. Moreover, we also provide simulation results for average spectral efficiency by considering AWGN and interference at both D and R to compare with that of the proposed interference-limited scenario. We consider the noise power spectral of -174 dBm/Hz [48]) and the same number of

[6]This is the residual SI power level after several stage of interference suppression at R. For example, considering the transmission power of $P_r = 30$ dBm, R requires -60 dB of SI suppression, which is feasible considering the current achievements in the FD research [23].

[7]Throughout this section, we consider the BER performance of the DPSK modulation.

$$\begin{aligned} C = {} & \frac{\Delta_r}{\ln(2)} G_{5,6}^{4,4}\left[\bar{\Psi}^2\bar{\beta}_y \middle| \begin{matrix} 0,0,1,1-m_y,1 \\ 0,0,k_w,m_w,1,0 \end{matrix}\right] + \frac{\Delta_d}{\ln(2)} G_{5,5}^{3,4}\left[\frac{\tilde{\beta}_u}{\bar{\beta}_v} \middle| \begin{matrix} 0,0,1,1-\tilde{m}_u,1 \\ 0,0,m_v,1,0 \end{matrix}\right] \\ & - \frac{\Delta_r\Delta_d}{\ln(2)} G_{2,2:3,4:2,3}^{2,1:2,3:1,2}\left[\bar{\Psi}^2\bar{\beta}_y, \frac{\tilde{\beta}_u}{\bar{\beta}_v} \middle| \begin{matrix} 0,1 \\ 0,0 \\ 0,1,1-m_y \\ k_w,m_w,1,0 \\ 1,1-\tilde{m}_u \\ m_v,0 \end{matrix}\right] - \frac{\Delta_r\Delta_d}{\ln(2)} G_{2,2:3,3:2,3}^{2,1:1,3:2,2}\left[\frac{\tilde{\beta}_u}{\bar{\beta}_v}, \bar{\Psi}^2\bar{\beta}_y \middle| \begin{matrix} 0,1 \\ 0,0 \\ 0,1,1-\tilde{m}_u \\ m_v,1,0 \\ 1,1-m_y \\ k_w,m_w,0 \end{matrix}\right] \end{aligned} \tag{20}$$

$$P_e = \frac{\Delta_r G_{3,3}^{2,3}\left[\frac{\bar{\Psi}^2\bar{\beta}_y}{q} \middle| \begin{matrix} 1,1-m_y,1-p \\ k_w,m_w,0 \end{matrix}\right]}{2\Gamma(p)} + \frac{\Delta_d G_{3,2}^{1,3}\left[\frac{\tilde{\beta}_u}{\bar{\beta}_v q} \middle| \begin{matrix} 1,1-\tilde{m}_u,1-p \\ m_v,0 \end{matrix}\right]}{2\Gamma(p)} - \frac{\Delta_r\Delta_d}{\bar{\gamma}} G_{1,0:2,3:2,2}^{0,1:2,2:1,2}\left[\frac{\bar{\Psi}^2\bar{\beta}_y}{q}, \frac{\tilde{\beta}_u}{\bar{\beta}_v q} \middle| \begin{matrix} 1-p \\ - \\ 1,1-m_y \\ k_w,m_w,0 \\ 1,1-\tilde{m}_u \\ m_v,0 \end{matrix}\right] \tag{22}$$

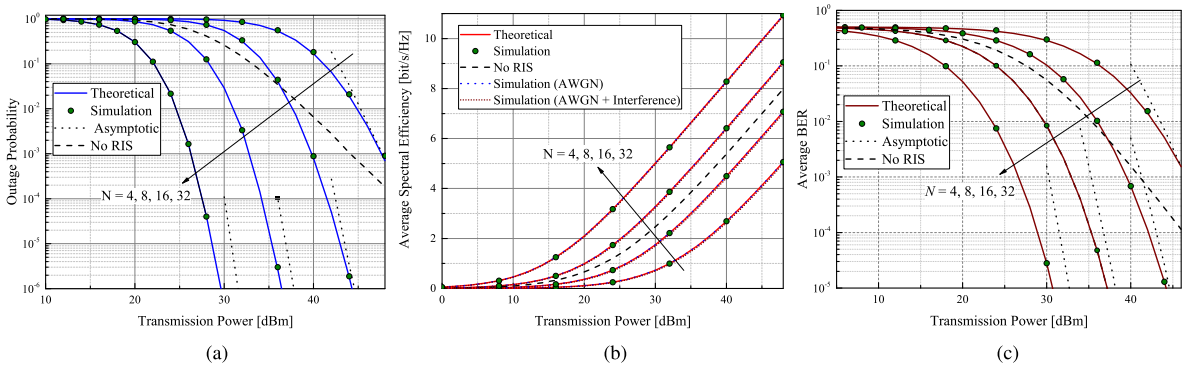

Fig. 3. Performance metrics versus transmission power for various RIS elements. (a) Outage probability. (b) Average spectral efficiency. (c) Average BER.

randomly located interference nodes $L = 5$ for R and D. First of all, we consider only the effect of AWGN on spectral efficiency by ignoring the impact of interference. It is clear from the curves (blue dot lines) that the effect of AWGN is negligible for all N. Furthermore, we can notice that the joint impact of AWGN and interference (short-dot brown lines) on spectral efficiency is minor. Another observation is that the impact of interference diminishes by increasing the number of RIS elements. These results justify our assumptions on AWGN and interference by showing that the proposed interference-limited system model achieves tight upper-bound results.

Furthermore, the RIS-aided FD network's performance enhancement in terms of the BER is shown in Fig. 3(c). Moreover, the asymptotic results derived in Section IV tightly converge to the exact analysis at high transmission power levels by confirming the accuracy of (17) and (23).

Next, we change the RIS location close to either S or R to identify the best RIS location that provides the maximum system performance for the considered system model. As shown in Fig. 4, the distance of the RIS on the x-axis is changed from 5 to 95 m. From the outage, spectral efficiency, and BER results in the plot, one can notice that the RIS provides better results when it is located closer to S or R. The minimum performance is obtained when the RIS is located in the middle of S and R. This phenomenon can be explained by the far-field channel modeling of the RIS, where the RIS link's path loss is inversely proportional to the multiplication of incoming and outgoing channel distances with power τ. For example, the path loss of the link through the RIS is higher when the RIS is located at an equal distance from S to D than the case when it is closer to one of the nodes. The RIS with $N = 4, 8$ cannot provide better system performance compared to the no-RIS model in Fig. 3. However, the outage [see Fig. 4(a)] and average spectral efficiency [see Fig. 4(b)] performance of the current system outperform those in Fig. 3 when the RIS is located closer to one of the nodes. Moreover, when $N > 16$, the RIS can be placed in any position to provide better performance than the no-RIS model.

Fig. 5 illustrates the impact of N and small-scale fading parameter m on the average BER performance at different RIS locations on the x-axis. Similar to [45] and [56], we assume LOS and NLOS mmWave links with $m = 2$ and $m = 4$, respectively. As expected, the system with $N = 24$ achieves better BER than that with $N = 16$. Moreover, it is observed that the increase in the parameter m results in the BER improvement. This happens because the parameter m represents the degree of fading severity of the channel. When $m = 1$, the channel experiences Rayleigh

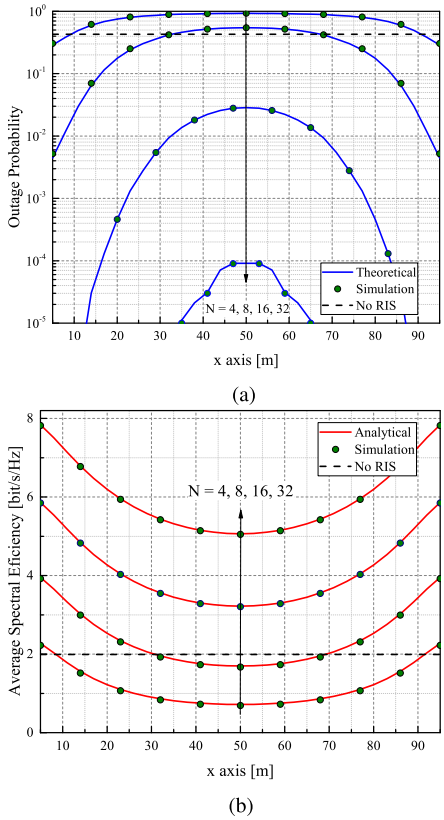

Fig. 4. Performance metrics versus distance for a various number of RIS elements with $P_s = P_r = 30$ dBm. (a) Outage probability. (b) Average spectral efficiency.

fading by providing the worse BER performance. Then, when the mmWave NLOS link ($m = 2$) is considered, the BER performance improves. However, the system achieves the best BER performance when the LOS channel is considered with $m = 4$. Another observation is that the impact of m is considerable on the BER performance for $N = 24$. For example, when $x = 50$ m, the BER enhancements between curves of $N = 16$ and $N = 24$ for $m = 1$ and $m = 4$ are 1.8 and 14 times, respectively.

Fig. 6 illustrates the OP results considering different residual SI levels at R. The plot highlights the importance of SI cancellation accuracy to guarantee the advantages of using the FD relay. For the considered transmit power, SI levels higher than

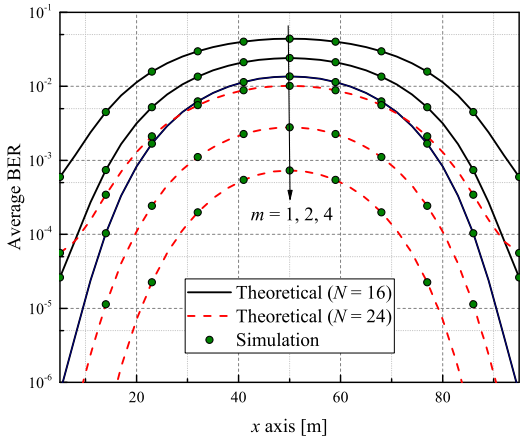

Fig. 5. Average BER versus distance for a various number of RIS elements and m parameters, with $P_s = P_r = 30$ dBm.

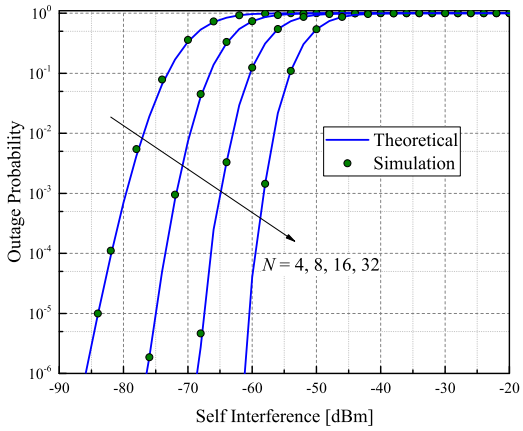

Fig. 6. OP versus residual SI power at R for $P_s = P_r = 30$ dBm and various N.

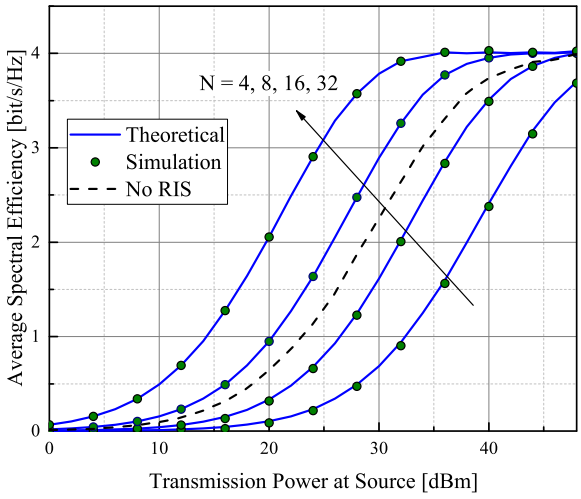

Fig. 7. Average spectral efficiency versus transmit power when $P_r = 0$ dBm.

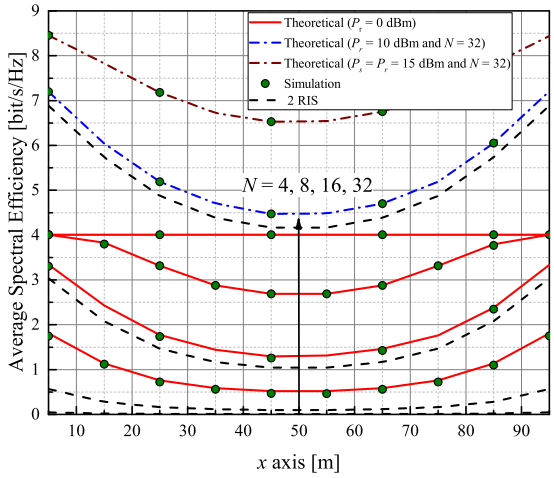

Fig. 8. Average spectral efficiency versus distance considering different N and transmission power.

-50 dBm cause a full outage to the system for any value of N. On the other hand, a certain OP can be achieved at different SI levels for various N. For example, the OP of 10^{-4} can be attained at the residual SI of -82 dBm for $N = 4$. The same OP can be achieved at -60 dBm for $N = 32$. In other words, the RIS with a higher number of reflecting elements can still improve the performance of the FD relay with considerable residual SI power. Considering these results, it may be less costly to employ the RIS with large N than design an FD relay with a high SI cancellation ability for obtaining certain QoS.

Fig. 7 plots the average spectral efficiency results considering a fixed transmission power at R, i.e., $P_r = 0$ dBm. From the results, we can observe that the spectral efficiency curves saturate at 4 bits/s/Hz for all N values. This happens since the end-to-end average spectral efficiency is restricted to $\min(\gamma_R, \gamma_D)$. Moreover, as derived in Section IV, the Nakagami-m parameter (m_v) of the R–D link is one of the parameters that define the diversity order. Hence, the achieved SIR at D becomes a bottleneck for the end-to-end spectral efficiency performance when the SIR at R gets higher. Therefore, it can be asserted that the use of the RIS with $N > 32$ does not provide spectral efficiency enhancement at higher transmission power for the considered system setup.

In Fig. 8, we compare the proposed FD-RIS model (Model I) with a similar setup where the FD relay is replaced with another RIS model. In the latter model, S transmits the signal to D through the two cascaded RISs (Model II). The transmit power at S for this simulation is 30 dBm. When $P_r = 0$ dBm and $N \leq 16$, it is obvious from the plot that Model I obtains a much better average spectral efficiency than Model II. However, when $N = 32$, the performance of Model I saturates at 4 bit/s/Hz, while the increase in the number of elements provides spectral efficiency improvements for Model II by achieving the maximum average spectral efficiency of 6.8 bit/s/Hz. Furthermore, when the transmit power at R is increased to $P_r = 10$ dBm and $N = 32$, the spectral efficiency performance of Model I outperforms the result of Model II. Hence, these results show that the FD relay can considerably enhance the system performance with higher transmission power. Besides, Fig. 8 also demonstrates the results when both the models have the same transmit power consumption.[8] Considering a total available transmit power of 30 dBm, Model I uses that power at S ($P_s = 30$ dBm), while, in Model II, S and R use half of that power ($P_s = P_r = 15$ dBm). The result shows that Model I achieves 1.57 bits/s/Hz better

[8]Here, we consider only the total transmit power used at each model. Bidirectional voltage translators, level regulators, etc., at RIS can consume power up to 1 W [57]. Hence, we ignore the consumed power at the RIS and R in this comparison.

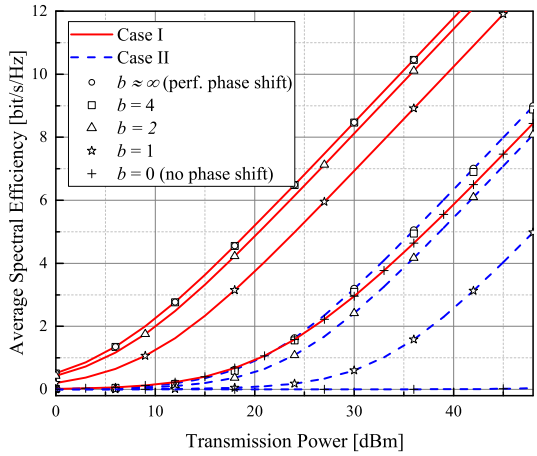

Fig. 9. Average spectral efficiency versus transmit power for Cases I and II.

TABLE II
COORDINATES OF NODES ILLUSTRATED IN FIG. 2

Nodes	x-axis	y-axis	Nodes	x-axis	y-axis
S	0	0	RIS C	100	0
RIS A	50	20	RIS B	150	20
R	100	0	D	200	0

average spectral efficiency than Model II in their maximum achieved performance. These results can infer that an intermediate FD relay provides better spectral efficiency performance than cascaded RISs due to the latter model's strong channel path loss.

Fig. 9 illustrates the average spectral efficiency performance for Cases I and II shown in Fig. 2. Apart from the previous results, herein, we consider an imperfect phase shift at RISs as

$$\theta_n = \left\{ e^{\frac{j2\pi l}{2^b}} \right\}_{l=0}^{2^b-1} \tag{24}$$

where b is the bit resolution of the RIS element's phase shifter. The coordinates for nodes are shown in Table II. Moreover, all the RISs have the same reflecting elements $N = 32$. We observe that the spectral efficiency curves for Case I considerably outperform those for Case II. For example, when $P_s = 30$ dBm and the phase-shift resolution $b \to \infty$, which corresponds to the perfect cophasing of the RIS phase shift, Case I attains 8.5 bit/s/Hz, while Case II achieves 3.1 bit/s/Hz (2.7 times lower). The lower spectral efficiency performance of Case II is due to the far-field path-loss effect of the cascaded four-hop distance of RISs [see (13)]. Moreover, we can observe that, when $b = 4$, the curve of Case I tightly converges with the perfect phase-shift performance. Furthermore, when the RIS has less phase-shift resolutions $b = 1$ and $b = 2$, the respective spectral efficiency performance drops from the ideal phase shift are 4.5% and 18.8%, respectively. Moreover, in the setup when the RIS performs no phase shifting ($b = 0$), the spectral efficiency degradation from the ideal phase-shift setup is 66%. Regarding Case II performance, we can see that the system setup with $b = 4$ does not provide tight results to reach the ideal system setup's performance with $b \to \infty$. Another observation is that the use of smaller phase-shift resolution considerably degrades the spectral efficiency performance. For example, compared with the spectral efficiency result of the ideal phase-shift curve at 30 dBm, the performance drop of the curve with $b = 1$ and $b = 2$ is 81% and 24%, respectively. If the RIS is set with no phase-shift ability ($b = 0$), then no QoS is achieved for Case II with the considered system settings. The obtained results from this plot support that using an intermediate FD relay as a repeater/booster in the RIS-based networks can further enhance the system performance by diminishing the path-loss impact of cascaded RIS links.

VI. CONCLUSION

This article studied the performance of RIS-aided dual-hop FD relaying networks. Exact analytical derivations for the OP, average spectral efficiency, and average BER were derived in closed forms. Moreover, asymptotic expressions were derived and the system diversity order was identified as a function of the number of the RIS elements N and channel shape parameter m. An increase in N improved the aforementioned end-to-end system performance. On the other hand, at a large value of N, the considered end-to-end system performance becomes dependent on the R–D link. Moreover, we numerically studied the cascaded multihop RIS system. The results showed that the increase in the number of RISs within the communication link does not provide substantial spectral efficiency improvement due to the RIS channel's far-field path-loss model. However, the RIS network could achieve better system performance when an intermediate DF-FD relaying node was inserted to combat the path-loss effect. The proposed RIS model with active FD relay can be extended in future works considering MIMO and multiuser systems.

APPENDIX A
PROOF OF LEMMA 1

The CDF of γ_R in (15) can be further written as

$$F_{\gamma_R}(\bar{\gamma}) = \Pr\left[\frac{\gamma}{Y} < \bar{\gamma}\right] = \int_0^\infty f_Y(y) F_\gamma(y\bar{\gamma}) dy$$
$$= \frac{\Delta_r}{\bar{\beta}_y} \int_0^\infty y^{m_y-1} e^{-\frac{y}{\bar{\beta}_y}} G_{1,3}^{2,1}\left[y\bar{\gamma}\bar{\Psi}^2 \middle| \begin{matrix} 1 \\ k_w, m_w, 0 \end{matrix} \right] dy \tag{A.1}$$

where $\Delta_r = \frac{1}{\Gamma(k_w)\Gamma(m_w)\Gamma(m_y)}$. Furthermore, applying [58, eq. (11)] into (A.1) and, then, using [58, eq. (21)], (A.1) can be written in closed form as

$$F_{\gamma_R}(\bar{\gamma}) = \frac{\Delta_r}{\bar{\beta}_y} \int_0^\infty y^{m_y-1} G_{0,1}^{1,0}\left[\frac{y}{\bar{\beta}_y} \middle| \begin{matrix} - \\ 0 \end{matrix} \right] G_{1,3}^{2,1}\left[\frac{\bar{\gamma}y}{\bar{\Psi}^{-2}} \middle| \begin{matrix} 1 \\ k_w, m_w, 0 \end{matrix} \right] dy$$
$$= \Delta_r G_{2,3}^{2,2}\left[\bar{\gamma}\bar{\Psi}^2\bar{\beta}_y \middle| \begin{matrix} 1, 1-m_y \\ k_w, m_w, 0 \end{matrix} \right]. \tag{A.2}$$

Similarly, we can write the CDF of γ_D in (15) as

$$F_{\gamma_D}(\bar{\gamma}) = \Pr\left[\frac{V}{U} < \bar{\gamma}\right] = \int_0^\infty f_U(u) F_V(\bar{\gamma}u) du$$
$$= \frac{\Delta_d}{\tilde{\beta}_u^{\tilde{m}_u}} \int_0^\infty u^{\tilde{m}_u-1} e^{-\frac{u}{\tilde{\beta}_u}} \gamma\left(m_v, \frac{\bar{\gamma}u}{\bar{\beta}_v} \right) du \tag{A.3}$$

where $\Delta_d = \frac{1}{\Gamma(m_v)\Gamma(\tilde{m}_u)}$, and $\gamma(a, b)$ is the lower incomplete gamma function [46, eq. (8.350.1)]. Furthermore, by applying [58, eq. (11)] and [53, eq. (06.07.26.0006.01)] into (A.3),

$F_{\gamma_D}(\bar{\gamma})$ can be further derived as

$$F_{\gamma_D}(\bar{\gamma}) = \frac{\Delta_d}{\bar{\beta}_u^{\tilde{m}_u}} \int_0^\infty u^{\tilde{m}_u - 1} G_{0,1}^{1,0}\left[\frac{u}{\bar{\beta}_u}\middle| \begin{matrix} - \\ 0 \end{matrix}\right] \times G_{1,2}^{1,1}\left[\frac{\bar{\gamma}}{\bar{\beta}_v} u \middle| \begin{matrix} 1 \\ m_v, 0 \end{matrix}\right] du = \Delta_d G_{2,2}^{1,2}\left[\frac{\tilde{\beta}_u}{\bar{\beta}_v}\bar{\gamma}\middle| \begin{matrix} 1, 1-\tilde{m}_u \\ m_v, 0 \end{matrix}\right]. \quad \text{(A.4)}$$

Finally, the OP at D is obtained by substituting (A.2) and (A.4) into (15) and written as in (16). ■

Appendix B
Proof of Lemma 2

The PDFs $f_R(\bar{\gamma})$ and $f_D(\bar{\gamma})$ in (19) are calculated by taking the derivative of (A.2) and (A.4) with respect to $\bar{\gamma}$. Hence, with the help of [53, eq. (07.34.20.0017.02)], we can write the PDFs as follows:

$$f_R(\bar{\gamma}) = \frac{\Delta_r}{\bar{\gamma}} G_{3,4}^{2,3}\left[\bar{\Psi}^2 \bar{\beta}_y \bar{\gamma}\middle| \begin{matrix} 0, 1, 1-m_y \\ k_w, m_w, 1, 0 \end{matrix}\right] \quad \text{(B.1)}$$

$$f_D(\bar{\gamma}) = \frac{\Delta_d}{\bar{\gamma}} G_{3,3}^{1,3}\left[\frac{\tilde{\beta}_u}{\bar{\beta}_v}\bar{\gamma}\middle| \begin{matrix} 0, 1, 1-\tilde{m}_u \\ m_v, 1, 0 \end{matrix}\right]. \quad \text{(B.2)}$$

Now, using the representation of $\ln(1+x) = G_{2,2}^{1,2}\left[x\middle|\begin{smallmatrix}1,1\\1,0\end{smallmatrix}\right]$ [58, eq. (11)] and (19), the average spectral efficiency can be rewritten as

$$C = \frac{1}{\ln(2)} \int_0^\infty G_{2,2}^{1,2}\left[\bar{\gamma}\middle|\begin{matrix}1,1\\1,0\end{matrix}\right] f_\gamma(\bar{\gamma}) d\bar{\gamma} = I_1 + I_2 - I_3 - I_4. \quad \text{(B.3)}$$

Using (B.1), the term I_1 in (B.3) can be further expanded as

$$I_1 = \frac{\Delta_r}{\ln(2)} \int_0^\infty \bar{\gamma}^{-1} G_{2,2}^{1,2}\left[\bar{\gamma}\middle|\begin{matrix}1,1\\1,0\end{matrix}\right] G_{3,4}^{2,3}\left[\frac{\bar{\beta}_y \bar{\gamma}}{\bar{\Psi}^{-2}}\middle|\begin{matrix}0,1,1-m_y\\k_w, m_w, 1, 0\end{matrix}\right] d\bar{\gamma} \overset{\bar{a}}{=} \frac{\Delta_r}{\ln(2)} G_{5,6}^{4,4}\left[\bar{\Psi}^2\bar{\beta}_y\middle|\begin{matrix}0,0,1,1-m_y,1\\0,0,k_w,m_w,1,0\end{matrix}\right] \quad \text{(B.4)}$$

where $\bar{a}$ is derived by consequential use of [46, eq. (9.31.5)] and [46, eq. (7.811.1)]. Similarly, considering $(B.2)$, the term I_2 can be derived as

$$I_2 = \frac{\Delta_d}{\ln(2)} \int_0^\infty \bar{\gamma}^{-1} G_{2,2}^{1,2}\left[\bar{\gamma}\middle|\begin{matrix}1,1\\1,0\end{matrix}\right] G_{3,3}^{1,3}\left[\frac{\tilde{\beta}_u}{\bar{\beta}_v}\bar{\gamma}\middle|\begin{matrix}0,1,1-\tilde{m}_u\\m_v,1,0\end{matrix}\right] d\bar{\gamma} = \frac{\Delta_d}{\ln(2)} G_{5,5}^{3,4}\left[\frac{\tilde{\beta}_u}{\bar{\beta}_v}\middle|\begin{matrix}0,0,1,1-\tilde{m}_u,1\\0,0,m_v,1,0\end{matrix}\right]. \quad \text{(B.5)}$$

Furthermore, using (A.3) and (B.1), the term I_3 can be found as

$$I_3 = \frac{\Delta_r \Delta_d}{\ln(2)} \int_0^\infty \bar{\gamma}^{-1} G_{2,2}^{1,2}\left[\bar{\gamma}\middle|\begin{matrix}1,1\\1,0\end{matrix}\right] \times G_{3,4}^{2,3}\left[\bar{\Psi}^2\bar{\beta}_y\bar{\gamma}\middle|\begin{matrix}0,1,1-m_y\\k_w,m_w,1,0\end{matrix}\right] G_{2,2}^{1,2}\left[\frac{\tilde{\beta}_u}{\bar{\beta}_v}\bar{\gamma}\middle|\begin{matrix}1,1-\tilde{m}_u\\m_v,0\end{matrix}\right] d\bar{\gamma} \overset{\bar{b}}{=} \frac{\Delta_r\Delta_d}{\ln(2)} G_{2,2:3,4:2,3}^{2,1:2,3:1,2}\left[\bar{\Psi}^2\bar{\beta}_y, \frac{\tilde{\beta}_u}{\bar{\beta}_v}\middle|\begin{matrix}0,1\\0,0\\0,1,1-m_y\\k_w,m_w,1,0\\1,1-\tilde{m}_u\\m_v,0\end{matrix}\right] \quad \text{(B.6)}$$

where $\bar{b}$ is derived using [53, eq. (07.34.21.0081.01)], and $G_{\cdot,\cdot:\cdot,\cdot:\cdot,\cdot}^{\cdot,\cdot:\cdot,\cdot:\cdot,\cdot}[\cdot]$ is the bivariate Meijer G-function, which can be calculated in MATLAB by using the approach in [59]. Then, using (A.2) and (B.2), the term I_4 can be obtained as

$$I_4 = \frac{\Delta_r\Delta_d}{\ln(2)} \int_0^\infty \bar{\gamma}^{-1} G_{2,2}^{1,2}\left[\bar{\gamma}\middle|\begin{matrix}1,1\\1,0\end{matrix}\right] G_{3,3}^{1,3}\left[\frac{\tilde{\beta}_u}{\bar{\beta}_v}\bar{\gamma}\middle|\begin{matrix}0,1,1-\tilde{m}_u\\m_v,1,0\end{matrix}\right] \times G_{2,3}^{2,2}\left[\bar{\Psi}^2\bar{\beta}_y\bar{\gamma}\middle|\begin{matrix}1,1-m_y\\k_w,m_w,0\end{matrix}\right] d\bar{\gamma} = \frac{\Delta_r\Delta_d}{\ln(2)} G_{2,2:3,3:2,3}^{2,1:1,3:2,2}\left[\frac{\tilde{\beta}_u}{\bar{\beta}_v}, \bar{\Psi}^2\bar{\beta}_y\middle|\begin{matrix}0,1\\0,0\\0,1,1-\tilde{m}_u\\m_v,1,0\\1,1-m_y\\k_w,m_w,0\end{matrix}\right]. \quad \text{(B.7)}$$

The end-to-end average spectral deficiency can be derived by substituting (B.4)–(B.7) into (B.3) and then written as (20). ■

Appendix C
Proof of Lemma 3

Using (15), we can further write (21) as follows:

$$P_e = \frac{q^p}{2\Gamma(p)} \int_0^\infty \bar{\gamma}^{p-1} e^{-q\bar{\gamma}} \left(F_{\gamma_R}(\bar{\gamma}) + F_{\gamma_D}(\bar{\gamma}) - F_{\gamma_R}(\bar{\gamma}) F_{\gamma_D}(\bar{\gamma})\right) d\bar{\gamma} = L_1 + L_2 - L_3. \quad \text{(C.1)}$$

Now, with the help of [58, eq. (11)] and (A.1), the term L_1 is written as

$$L_1 = \frac{\Delta_r q^p}{2\Gamma(p)} \int_0^\infty \bar{\gamma}^{p-1} G_{0,1}^{1,0}\left[q\bar{\gamma}\middle|\begin{matrix}-\\0\end{matrix}\right] G_{2,3}^{2,2}\left[\bar{\Psi}^2\bar{\beta}_y\bar{\gamma}\middle|\begin{matrix}1,1-m_y\\k_w,m_w,0\end{matrix}\right] d\bar{\gamma} \overset{\bar{c}}{=} \frac{\Delta_r}{2\Gamma(p)} G_{3,3}^{2,3}\left[\frac{\bar{\Psi}^2\bar{\beta}_y}{q}\middle|\begin{matrix}1,1-m_y,1-p\\k_w,m_w,0\end{matrix}\right] \quad \text{(C.2)}$$

where $\bar{c}$ is derived using [58, eq. (21)]. Similarly, using (A.3), the term I_2 is calculated as

$$L_2 = \frac{\Delta_d q^p}{2\Gamma(p)} \int_0^\infty \bar{\gamma}^{p-1} G_{0,1}^{1,0}\left[q\bar{\gamma}\middle|\begin{matrix}-\\0\end{matrix}\right] G_{2,2}^{1,2}\left[\frac{\tilde{\beta}_u\bar{\gamma}}{\bar{\beta}_v}\middle|\begin{matrix}1,1-\tilde{m}_u\\m_v,0\end{matrix}\right] d\bar{\gamma} = \frac{\Delta_d}{2\Gamma(p)} G_{3,2}^{1,3}\left[\frac{\tilde{\beta}_u}{\bar{\beta}_v q}\middle|\begin{matrix}1,1-\tilde{m}_u,1-p\\m_v,0\end{matrix}\right]. \quad \text{(C.3)}$$

Finally, using (A.2) and (A.3) and applying [53, eq. (07.34.21.0081.01)], the term L_3 can be further written as

$$L_3 = \frac{\Delta_r\Delta_d q^p}{2\Gamma(p)} \int_0^\infty \bar{\gamma}^{p-1} G_{0,1}^{1,0}\left[q\bar{\gamma}\middle|\begin{matrix}-\\0\end{matrix}\right] \times G_{2,3}^{2,2}\left[\bar{\Psi}^2\bar{\beta}_y\bar{\gamma}\middle|\begin{matrix}1,1-m_y\\k_w,m_w,0\end{matrix}\right] G_{2,2}^{1,2}\left[\frac{\tilde{\beta}_u}{\bar{\beta}_v}\bar{\gamma}\middle|\begin{matrix}1,1-\tilde{m}_u\\m_v,0\end{matrix}\right] d\bar{\gamma}$$

$$= \frac{\Delta_r \Delta_d}{\bar{\gamma}} G_{1,0:2,3:2,2}^{0,1:2,2:1,2} \left[\frac{\bar{\Psi}^2 \bar{\beta}_y}{q}, \frac{\tilde{\beta}_u}{\bar{\beta}_v q} \middle| \begin{matrix} 1-p \\ - \\ 1, 1-m_y \\ k_w, m_w, 0 \\ 1, 1-\tilde{m}_u \\ m_v, 0 \end{matrix} \right]. \quad \text{(C.4)}$$

Finally, the end-to-end average BER can be derived by substituting (C.2)–(C.4) into (C.1) and written as in (22). ■

REFERENCES

[1] *IMT Vision—Framework and Overall Objectives of the Future Development of IMT for 2020 and Beyond*, ITU-R, Geneva, Switzerland, Sep. 2015.

[2] C. Pan, M. Elkashlan, J. Wang, J. Yuan, and L. Hanzo, "User-centric C-RAN architecture for ultra-dense 5G networks: Challenges and methodologies," *IEEE Commun. Mag.*, vol. 56, no. 6, pp. 14–20, Jun. 2018.

[3] J. Zhang, X. Ge, Q. Li, M. Guizani, and Y. Zhang, "5G millimeter-wave antenna array: Design and challenges," *IEEE Wireless Commun.*, vol. 24, no. 2, pp. 106–112, 2017.

[4] Z. Lin, M. Lin, T. de Cola, J.-B. Wang, W.-P. Zhu, and J. Cheng, "Supporting IoT with rate-splitting multiple access in satellite and aerial-integrated networks," *IEEE Internet Things J.*, vol. 8, no. 14, pp. 11123–11134, Jul. 2021.

[5] T. S. Rappaport et al., "Wireless communications and applications above 100 GHz: Opportunities and challenges for 6G and beyond," *IEEE Access*, vol. 7, pp. 78729–78757, 2019.

[6] T. S. Rappaport, J. N. Murdock, and F. Gutierrez, "State of the art in 60-GHz integrated circuits and systems for wireless communications," *Proc. IEEE*, vol. 99, no. 8, pp. 1390–1436, Aug. 2011.

[7] M. Nemati, J. Park, and J. Choi, "RIS-assisted coverage enhancement in millimeter-wave cellular networks," *IEEE Access*, vol. 8, pp. 188171–188185, 2020.

[8] M. A. ElMossallamy, H. Zhang, L. Song, K. G. Seddik, Z. Han, and G. Y. Li, "Reconfigurable intelligent surfaces for wireless communications: Principles, challenges, and opportunities," *IEEE Trans. Cogn. Commun. Netw.*, vol. 6, no. 3, pp. 990–1002, Sep. 2020.

[9] L. Dai et al., "Reconfigurable intelligent surface-based wireless communications: Antenna design, prototyping, and experimental results," *IEEE Access*, vol. 8, pp. 45913–45923, 2020.

[10] X. Tan, Z. Sun, D. Koutsonikolas, and J. M. Jornet, "Enabling indoor mobile millimeter-wave networks based on smart reflect-arrays," in *Proc. IEEE Conf. Comput. Commun.*, 2018, pp. 270–278.

[11] J. Yuan, Y. Liang, J. Joung, G. Feng, and E. G. Larsson, "Intelligent reflecting surface (IRS)-enhanced cognitive radio system," in *Proc. IEEE Int. Conf. Commun.*, 2020, pp. 1–6.

[12] Y. Zheng, S. Bi, Y. J. Zhang, Z. Quan, and H. Wang, "Intelligent reflecting surface enhanced user cooperation in wireless powered communication networks," *IEEE Wireless Commun. Lett.*, vol. 9, no. 6, pp. 901–905, Jun. 2020.

[13] M. Makin, G. Nauryzbayev, S. Arzykulov, and M. S. Hashmi, "Performance of large intelligent surface-enabled cooperative networks over Nakagami-m channels," in *Proc. IEEE 94th Veh. Technol. Conf.*, 2021, pp. 1–6.

[14] J. Qiao and M. S. Alouini, "Secure transmission for intelligent reflecting surface-assisted mmWave and terahertz systems," *IEEE Wireless Commun. Lett.*, vol. 9, no. 10, pp. 1743–1747, Oct. 2020.

[15] E. Bjornson, O. Ozdogan, and E. G. Larsson, "Intelligent reflecting surface versus decode-and-forward: How large surfaces are needed to beat relaying?," *IEEE Wireless Commun. Lett.*, vol. 9, no. 2, pp. 244–248, Feb. 2020.

[16] M. Di Renzo et al., "Reconfigurable intelligent surfaces vs. relaying: Differences, similarities, and performance comparison," *IEEE Open J. Commun. Soc.*, vol. 1, pp. 798–807, 2020.

[17] W. Tang et al., "Wireless communications with reconfigurable intelligent surface: Path loss modeling and experimental measurement," *IEEE Trans. Wireless Commun.*, vol. 20, no. 1, pp. 421–439, Jan. 2021.

[18] D. Kim, H. Lee, and D. Hong, "A survey of in-band full-duplex transmission: From the perspective of PHY and MAC layers," *IEEE Commun. Surv. Tuts.*, vol. 17, no. 4, pp. 2017–2046, Fourth Quarter 2015.

[19] G. Nauryzbayev, M. Abdallah, and K. M. Rabie, "Outage probability of the EH-based full-duplex AF and DF relaying systems in $\alpha - \mu$ environment," in *Proc. IEEE 88th Veh. Technol. Conf.*, 2018, pp. 1–6.

[20] K. Rabie, B. Adebisi, G. Nauryzbayev, O. S. Badarneh, X. Li, and M.-S. Alouini, "Full-duplex energy-harvesting enabled relay networks in generalized fading channels," *IEEE Wireless Commun. Lett.*, vol. 8, no. 2, pp. 384–387, Apr. 2019.

[21] E. Everett, A. Sahai, and A. Sabharwal, "Passive self-interference suppression for full-duplex infrastructure nodes," *IEEE Trans. Wireless Commun.*, vol. 13, no. 2, pp. 680–694, Feb. 2014.

[22] E. Ahmed and A. M. Eltawil, "All-digital self-interference cancellation technique for full-duplex systems," *IEEE Trans. Wireless Commun.*, vol. 14, no. 7, pp. 3519–3532, Jul. 2015.

[23] D. Bharadia, E. McMilin, and S. Katti, "Full duplex radios," in *Proc. ACM SIGCOMM Conf.*, 2013, pp. 375–386.

[24] S. Silva, M. Ardakani, and C. Tellambura, "Relay selection for cognitive massive MIMO two-way relay networks," in *Proc. IEEE Wireless Commun. Netw. Conf.*, 2017, pp. 1–6.

[25] S. Atapattu, Y. Jing, H. Jiang, and C. Tellambura, "Relay selection schemes and performance analysis approximations for two-way networks," *IEEE Trans. Commun.*, vol. 61, no. 3, pp. 987–998, Mar. 2013.

[26] Z. Zhang, Z. Chen, M. Shen, and B. Xia, "Spectral and energy efficiency of multipair two-way full-duplex relay systems with massive MIMO," *IEEE J. Sel. Areas Commun.*, vol. 34, no. 4, pp. 848–863, Apr. 2016.

[27] S. Gong, C. Xing, Z. Fei, and S. Ma, "Millimeter-wave secrecy beamforming designs for two-way amplify-and-forward MIMO relaying networks," *IEEE Trans. Veh. Technol.*, vol. 66, no. 3, pp. 2059–2071, Mar. 2017.

[28] P. K. Sharma and P. Garg, "Intelligent reflecting surfaces to achieve the full-duplex wireless communication," *IEEE Commun. Lett.*, vol. 25, no. 2, pp. 622–626, Feb. 2021.

[29] H. Shen, T. Ding, W. Xu, and C. Zhao, "Beamforming design with fast convergence for IRS-aided full-duplex communication," *IEEE Commun. Lett.*, vol. 24, no. 12, pp. 2849–2853, Dec. 2020.

[30] D. Xu, X. Yu, Y. Sun, D. W. K. Ng, and R. Schober, "Resource allocation for IRS-assisted full-duplex cognitive radio systems," *IEEE Trans. Commun.*, vol. 68, no. 12, pp. 7376–7394, Dec. 2020.

[31] Z. Peng, Z. Zhang, C. Pan, L. Li, and A. L. Swindlehurst, "Multiuser full-duplex two-way communications via intelligent reflecting surface," *IEEE Trans. Signal Process.*, vol. 69, pp. 837–851, 2021.

[32] S. Atapattu, R. Fan, P. Dharmawansa, G. Wang, J. Evans, and T. A. Tsiftsis, "Reconfigurable intelligent surface assisted two-way communications: Performance analysis and optimization," *IEEE Trans. Commun.*, vol. 68, no. 10, pp. 6552–6567, Oct. 2020.

[33] K. Tian, B. Duo, S. Li, Y. Zuo, and X. Yuan, "Hybrid uplink and downlink transmissions for full-duplex UAV communication with RIS," *IEEE Wireless Commun. Lett.*, vol. 11, no. 4, pp. 866–870, Apr. 2022.

[34] W. Khalid, H. Yu, D.-T. Do, Z. Kaleem, and S. Noh, "RIS-aided physical layer security with full-duplex jamming in underlay D2D networks," *IEEE Access*, vol. 9, pp. 99667–99679, 2021.

[35] Y. Ge and J. Fan, "Robust secure beamforming for intelligent reflecting surface assisted full-duplex MISO systems," *IEEE Trans. Inf. Forensics Secur.*, vol. 17, pp. 253–264, 2022.

[36] M. Elhattab, M. A. Arfaoui, C. Assi, and A. Ghrayeb, "Reconfigurable intelligent surface enabled full-duplex/half-duplex cooperative non-orthogonal multiple access," *IEEE Trans. Wireless Commun.*, vol. 21, no. 5, pp. 3349–3364, May 2022.

[37] Z. Abdullah, G. Chen, S. Lambotharan, and J. A. Chambers, "Optimization of intelligent reflecting surface assisted full-duplex relay networks," *IEEE Wireless Commun. Lett.*, vol. 10, no. 2, pp. 363–367, Feb. 2021.

[38] X. Ying, U. Demirhan, and A. Alkhateeb, "Relay aided intelligent reconfigurable surfaces: Achieving the potential without so many antennas," Jun. 2020, *arXiv:2006.06644*.

[39] I. Yildirim, A. Uyrus, and E. Basar, "Modeling and analysis of reconfigurable intelligent surfaces for indoor and outdoor applications in future wireless networks," *IEEE Trans. Commun.*, vol. 69, no. 2, pp. 1290–1301, Feb. 2021.

[40] C. Huang et al., "Hybrid beamforming for RIS-empowered multi-hop terahertz communications: A DRL-based method," in *Proc. IEEE Globecom Workshops*, pp. 1–6.

[41] B. Zheng, C. You, and R. Zhang, "Double-IRS assisted multi-user MIMO: Cooperative passive beamforming design," *IEEE Trans. Wireless Commun.*, vol. 20, no. 7, pp. 4513–4526, Jul. 2021.

[42] L. Yang, F. Meng, Q. Wu, D. B. da Costa, and M. S. Alouini, "Accurate closed-form approximations to channel distributions of RIS-aided wireless systems," *IEEE Wireless Commun. Lett.*, vol. 9, no. 11, pp. 1985–1989, Nov. 2020.

[43] K. P. Peppas, "Accurate closed-form approximations to generalised-k sum distributions and applications in the performance analysis of equal-gain combining receivers," *IET Commun.*, vol. 5, pp. 982–989, May 2011.

[44] T. S. Rappaport et al., "Millimeter wave mobile communications for 5G cellular: It will work!," *IEEE Access*, vol. 1, pp. 335–349, 2013.
[45] S. Kusaladharma, Z. Zhang, and C. Tellambura, "Interference and outage analysis of random D2D networks underlaying millimeter-wave cellular networks," *IEEE Trans. Commun.*, vol. 67, no. 1, pp. 778–790, Jan. 2019.
[46] I. S. Gradshteyn and I. M. Ryzhik, *Table of Integrals, Series, and Products*, 7th ed. Amsterdam, The Netherlands: Elsevier/Academic, 2007.
[47] A. Goldsmith, *Wireless Communications*. Cambridge, U.K.: Cambridge Univ. Press, 2005.
[48] E. Björnson, H. Wymeersch, B. Matthiesen, P. Popovski, L. Sanguinetti, and E. de Carvalho, "Reconfigurable intelligent surfaces: A signal processing perspective with wireless applications," *IEEE Signal Process. Mag.*, vol. 39, no. 2, pp. 135–158, Mar. 2022.
[49] Y. Liu et al., "Reconfigurable intelligent surfaces: Principles and opportunities," *IEEE Commun. Surv. Tuts.*, vol. 23, no. 3, pp. 1546–1577, Third Quarter 2021.
[50] G. K. Karagiannidis, N. C. Sagias, and P. T. Mathiopoulos, "$N*$nakagami: A novel stochastic model for cascaded fading channels," *IEEE Trans. Commun.*, vol. 55, no. 8, pp. 1453–1458, Aug. 2007.
[51] S. Covo and A. Elalouf, "A novel single-gamma approximation to the sum of independent gamma variables, and a generalization to infinitely divisible distributions," *Electron. J. Statist.*, vol. 8, no. 1, pp. 894–926, 2014.
[52] S. Arzykulov, G. Nauryzbayev, A. Celik, and A. M. Eltawil, "Hardware and interference limited cooperative CR-NOMA networks under imperfect SIC and CSI," *IEEE Open J. Commun. Soc.*, vol. 2, pp. 1473–1485, 2021.
[53] *The Wolfram Functions Site*, Wolfram, Champaign, IL, USA, 2021.
[54] K. P. Peppas, A. N. Stassinakis, H. E. Nistazakis, and G. S. Tombras, "Capacity analysis of dual amplify-and-forward relayed free-space optical communication systems over turbulence channels with pointing errors," *J. Opt. Commun. Netw.*, vol. 5, pp. 1032–1042, Sep. 2013.
[55] L. Yang, J. Yang, W. Xie, M. O. Hasna, T. Tsiftsis, and M. D. Renzo, "Secrecy performance analysis of RIS-aided wireless communication systems," *IEEE Trans. Veh. Technol.*, vol. 69, no. 10, pp. 12296–12300, Oct. 2020.
[56] L. Tlebaldiyeva, B. Maham, and T. A. Tsiftsis, "Capacity analysis of device-to-device mmWave networks under transceiver distortion noise and imperfect CSI," *IEEE Trans. Veh. Technol.*, vol. 69, no. 5, pp. 5707–5712, May 2020 .
[57] X. Pei et al., "RIS-aided wireless communications: Prototyping, adaptive beamforming, and indoor/outdoor field trials," *IEEE Trans. Commun.*, vol. 69, no. 12, pp. 8627–8640, 2021, doi: 10.1109/TCOMM.2021.3116151.
[58] V. Adamchik and O. Marichev, "The algorithm for calculating integrals of hypergeometric type functions and its realization in REDUCE system," in *Proc. Int. Symp. Symbolic Algebr. Comput.*, 1990, pp. 212–224.
[59] H. Chergui, M. Benjillali, and S. Saoudi, "Performance analysis of project-and-forward relaying in mixed MIMO-pinhole and Rayleigh dual-hop channel," *IEEE Commun. Lett.*, vol. 20, no. 3, pp. 610–613, Mar. 2016.

Sultangali Arzykulov (Member, IEEE) received the B.Sc. (Hons.) degree in radio engineering, electronics, and telecommunications from Kazakh National Research Technical University, Almaty, Kazakhstan, in 2010, the M.Sc. degree in communication engineering from the University of Manchester, Manchester, U.K., in 2013, and the Ph.D. degree in science, engineering, and technology from Nazarbayev University, Nur-Sultan, Kazakhstan, in 2019.

He was a Postdoctoral Scholar with Nazarbayev University, from 2019 to 2020. He is currently a Postdoctoral Fellow with the King Abdullah University of Science and Technology, Thuwal, Saudi Arabia. His research interests include wireless communication systems, with particular focus on intelligent reconfigurable surface, cognitive radio, energy harvesting, interference mitigation, and nonorthogonal multiple access.

Dr. Arzykulov is a Reviewer for several international journals/conferences and was a Technical Program Committee Member of numerous IEEE Communication Society flagship conferences.

Galymzhan Nauryzbayev (Senior Member, IEEE) received the B.Sc. and M.Sc. degrees (Hons.) in radio engineering, electronics, and telecommunications from the Almaty University of Power Engineering and Telecommunication, Almaty, Kazakhstan, in 2009 and 2011, respectively, and the Ph.D. degree in wireless communications from the University of Manchester, Manchester, U.K., in 2016.

From 2016 to 2018, he held several academic and research positions with Nazarbayev University, Nur-Sultan, Kazakhstan, L.N. Gumilyov Eurasian National University, Astana, Kazakhstan, and Hamad Bin Khalifa University, Ar-Rayyan, Qatar. Since 2019, he has been an Assistant Professor with Nazarbayev University. His research interests include wireless communication systems, with a particular focus on reconfigurable intelligent surface-enabled communications, multiuser multiple-input multiple-output systems, cognitive radio, signal processing, energy harvesting, visible light communications, nonorthogonal multiple access, and interference mitigation.

Dr. Nauryzbayev is a Member of the National Research Council of the Republic of Kazakhstan. He was a Technical Program Committee Member of numerous IEEE flagship conferences.

Abdulkadir Celik (Senior Member, IEEE) received the M.S. degree in electrical engineering, the second M.S. degree in computer engineering, and the Ph.D. degree in co-majors of electrical engineering and computer engineering from Iowa State University, Ames, IA, USA, in 2013, 2015, and 2016, respectively.

From 2016 to 2020, he was a Postdoctoral Fellow with the King Abdullah University of Science and Technology, Thuwal, Saudi Arabia, where he is currently a Research Scientist with the Communication and Computing Systems Lab. His research interests include wireless communication systems and networks.

Ahmed M. Eltawil (Senior Member, IEEE) received the B.Sc. and M.Sc. degrees (Hons.) in electronics and communications engineering from Cairo University, Giza, Egypt, in 1997 and 1999, respectively, and the Doctorate degree in integrated circuits and systems from the University of California, Los Angeles, CA, USA, in 2003.

In August 2019, he joined the Computer, Electrical and Mathematical Sciences and Engineering Division, King Abdullah University of Science and Technology (KAUST), Thuwal, Saudi Arabia, where he is currently a Professor. Prior to that, he was a Professor with the Department of Electrical Engineering and Computer Science, University of California, Irvine, CA, USA. He has been on the technical program committees and steering committees for workshops, symposia, and conferences in the areas of low power computing, wireless communication system design, and cyber-physical systems (CPS). He is the Founder of the Communication and Computing Systems Lab, KAUST. His research interests include low-power digital circuit and signal processing architectures with an emphasis on mobile computing and communication systems and their applications, spanning wireless networks, personal networks, and CPS.

Dr. Eltawil received several awards, as well as distinguished grants, including the National Science Foundation CAREER Grant supporting his research in low power computing and communication systems, and the Henry Samueli School of Engineering, University of California, Irvine Innovator of the Year Award in 2021. He is a Senior Member of the National Academy of Inventors.